

Sum decomposition of Mueller-matrix images and spectra of beetle cuticles

Hans Arwin, Roger Magnusson, Enric Garcia-Caurel, C. Fallet, Kenneth Järrendahl, M. Foldyna, A. De Martino and R. Ossikovski

Linköping University Post Print



N.B.: When citing this work, cite the original article.

Original Publication:

Hans Arwin, Roger Magnusson, Enric Garcia-Caurel, C. Fallet, Kenneth Järrendahl, M. Foldyna, A. De Martino and R. Ossikovski, Sum decomposition of Mueller-matrix images and spectra of beetle cuticles, 2015, Optics Express, (23), 3, 1951-1966.

<http://dx.doi.org/10.1364/OE.23.001951>

Copyright: Optical Society of America

<http://www.osa.org/>

Postprint available at: Linköping University Electronic Press

<http://urn.kb.se/resolve?urn=urn:nbn:se:liu:diva-111944>

Sum decomposition of Mueller-matrix images and spectra of beetle cuticles

H. Arwin,^{1,*} R. Magnusson,¹ E. Garcia-Caurel,² C. Fallet,³
K. Järrendahl,¹ M. Foldyna,² A. De Martino,^{2,†} and
R. Ossikovski²

¹Laboratory of Applied Optics, Department of Physics, Chemistry and Biology, Linköping University, SE-581 83 Linköping, Sweden

²Laboratoire des Physique des Interfaces et Couches Minces, Ecole Polytechnique, CNRS, F-91128 Palaiseau, France

³Bioaxial SAS, 40 rue de Paradis, F-75010 Paris, France

[†]August 23, 2014

^{*}han@ifm.liu.se

Abstract: Spectral Mueller matrices measured at multiple angles of incidence as well as Mueller matrix images are recorded on the exoskeletons (cuticles) of the scarab beetles *Cetonia aurata* and *Chrysina argenteola*. *Cetonia aurata* is green whereas *Chrysina argenteola* is gold-colored. When illuminated with natural (unpolarized) light, both species reflect left-handed and near-circularly polarized light originating from helicoidal structures in their cuticles. These structures are referred to as circular Bragg reflectors. For both species the Mueller matrices are found to be nondiagonal depolarizers. The matrices are Cloude decomposed to a sum of non-depolarizing matrices and it is found that the cuticle optical response, in a first approximation can be described as a sum of Mueller matrices from an ideal mirror and an ideal circular polarizer with relative weights determined by the eigenvalues of the covariance matrices of the measured Mueller matrices. The spectral and image decompositions are consistent with each other. A regression-based decomposition of the spectral and image Mueller matrices is also presented whereby the basic optical components are assumed to be a mirror and a circular polarizer as suggested by the Cloude decomposition. The advantage with a regression decomposition compared to a Cloude decomposition is its better stability as the matrices in the decomposition are determined a priori. The origin of the depolarizing features are discussed but from present data it is not possible to conclude whether the two major components, the mirror and the circular polarizer are laterally separated in domains in the cuticle or if the depolarization originates from the intrinsic properties of the helicoidal structure.

© 2015 Optical Society of America

OCIS codes: (160.1585) Chiral media; (260.5430) Polarization; (260.2130) Ellipsometry and polarimetry; (160.4760) Optical properties.

References and links

1. D. H. Goldstein, "Polarization properties of Scarabaeidae," Appl. Opt. **45**, 7944–7950 (2006).
2. I. Hodgkinson, S. Lowrey, L. Bourke, A. Parker, and M. W. McCall, "Mueller-matrix characterization of beetle cuticle: polarized and unpolarized reflections from representative architectures," Appl. Opt. **49**, 4558–4567 (2010).

3. H. Arwin, R. Magnusson, J. Landin, and K. Järrendahl, "Chirality-induced polarization effects in the cuticle of scarab beetles: 100 years after Michelson," *Phil. Mag.* **92**, 1583–1599 (2012).
4. H. Arwin, T. Berlind, B. Johs, and K. Järrendahl, "Cuticle structure of the scarab beetle *Cetonia aurata* analyzed by regression analysis of Mueller-matrix ellipsometric data," *Opt. Express* **21**, 22645–22656 (2013).
5. R. Ossikovski, M. Anastasiadou, S. Ben Hatit, E. Garcia-Caurel, and A. De Martino, "Depolarizing Mueller matrices: how to decompose them?," *Phys. Status Solidi A* **205**, 720–727 (2008).
6. S. R. Cloude, "Group theory and polarization algebra," *Optik (Stuttgart)* **75**, 26–36 (1986).
7. S. R. Cloude and E. Pottier, "A review of target decomposition theorems in radar polarimetry," *IEEE Trans. Geosci. and Remote Sensing* **34**, 498–518 (1996).
8. R. Ossikovski, E. Garcia-Caurel, M. Foldyna, and J. J. Gil, "Application of the arbitrary decomposition to finite spot size Mueller matrix measurements," *Appl. Opt.* **53**, 6030–6036 (2014).
9. F. Le Roy-Bréhonnet, B. Le Jeune, P. Eliés, J. Cariou, and J. Lotrian, "Optical media and target characterization by Mueller matrix decomposition," *J. Phys. D: Appl. Phys.* **29**, 34–38 (1996).
10. M. Foldyna, E. Garcia-Caurel, R. Ossikovski, A. De Martino, and J. J. Gil, "Retrieval of a non-depolarizing component of experimentally determined depolarizing Mueller matrices," *Opt. Express* **17**, 12794–12806 (2009).
11. R. Ossikovski, M. Foldyna, C. Fallet, and A. De Martino, "Experimental evidence for naturally occurring non-diagonal depolarizers," *Opt. Lett.* **34**, 2426–2428 (2009).
12. S. Ben Hatit, M. Foldyna, A. De Martino, and B. Drevillon, "Angle-resolved Mueller polarimeter using a microscope objective," *Phys. Status Solidi A* **205**, 743–747 (2008).
13. C. Fallet, *Angle resolved Mueller polarimetry, applications to periodic structures* (PhD thesis, École polytechnique, 2012).
14. H. Arwin, L. Fernández del Río, and K. Järrendahl, "Comparison and analysis of Mueller-matrix spectra from exoskeletons of blue, green and red *Cetonia aurata*," *Thin Solid Films* **571**, 739–743 (2014).
15. E. Collett, *Polarized Light: Fundamentals and Applications*, Optical Engineering **21** (Marcel Dekker, Inc., 1992).
16. R. T. Holm, "Convention confusions," in *Handbook of Optical Constants of Solids II*, E. D. Palik, ed. (Academic Press, 1991), pp. 21–55.
17. V. Sharma, M. Crne, J. O. Park, and M. Srinivasarao, "Structural origin of circularly polarized iridescence in jeweled beetles," *Science* **325**, 449–451 (2009).
18. L. Fernández del Río, H. Arwin, and K. Järrendahl, "Polarizing properties and structural characteristics of the cuticle of the scarab beetle *Chrysina gloriosa*," *Thin Solid Films* **571**, 410–415 (2014).
19. R. Ossikovski, "Canonical forms of depolarizing Mueller matrices," *J. Opt. Soc. Am. A* **27**, 123–130 (2010).
20. A. Lakhtakia and M. McCall, "Simple expressions for Bragg reflection from axially excited chiral sculptured thin films," *J. Modern Opt.* **49**, 1525–1535 (2002).
21. E. Muñoz-Pineda, K. Järrendahl, H. Arwin, and A. Mendoza-Galván, "Symmetries and relationships between elements of the Mueller matrix spectra of the cuticle of the beetle *Cotinis mutabilis*," *Thin Solid Films* **571**, 660–665 (2014).
22. A. Mendoza-Galván, E. Muñoz-Pineda, K. Järrendahl, and H. Arwin, "Evidence for a dispersion relation of optical modes in the cuticle of the scarab beetle *Cotinis mutabilis*," *Opt. Mater. Express* **4**, 2484–2496 (2014).

1. Introduction

Mueller-matrix spectra of beetle cuticles have been reported by several authors. Goldstein [1] measured normal-incidence Mueller matrices on *Chrysina resplendens*, *Chrysina gloriosa* and *Chrysina clypealis* (In [1] the name *Plusiotis* is used instead of *Chrysina*). Hodgkinson et al. [2] and our group [3] have reported near-normal incidence and angle-dependent Mueller-matrices, respectively, and presented polarization features including both left-handed and right-handed near-circular polarization in reflection from several scarab beetle species. Derived parameters like ellipticity, handedness, degree of polarization, depolarization and more are reported. Recently we have also presented a regression analysis approach to extract structural information and cuticle refractive indices from Mueller-matrix data of the scarab beetle *Cetonia aurata* [4]. In this report we extend the study of Mueller matrices measured on beetles to an analysis of the fundamental properties of the matrices themselves by performing sum decompositions.

Decomposition of Mueller matrices are well described in the literature as reviewed by Ossikovski et al. [5]. Here we address *sum decomposition* of depolarizing Mueller matrices. Particularly we use the so called Cloude decomposition [6, 7] which will be described in some detail in the theory section. A Cloude decomposition can be applied to any depolarizing Mueller matrix. In some special cases with partially known forms of Mueller matrix components, a

decomposition into two different components can be done without an exact knowledge of any of them [8]. Another sum decomposition method has been described by Le Roy-Bréhonnet et al. [9]. However, the latter decomposition requires that three out of four possible eigenvalues of the covariance matrix derived from the measured Mueller matrix are the same. This method can be used to decompose a depolarizing matrix into a non-depolarizing matrix and a residual matrix considered to be noise.

Foldyna et al. [10] applied sum decomposition to a Mueller matrix measured in reflection mode with a beam spot covering two or three regions with different non-depolarizing Mueller matrices. As a demonstrator a silicon wafer with regions with diffraction gratings was used. Due to the mixture of Mueller matrices from different areas within the beam spot, the measured Mueller matrix was depolarizing. In the first example with two regions, one of the regions was characterized separately to determine its Mueller matrix and the second matrix could then be retrieved from the mixed data. In a second example two of three regions were first analyzed separately and then the properties of the third one could be retrieved. Another example of the use of sum decomposition was demonstrated by Ossikovski et al. [11]. They analyzed reflection Mueller-matrix images from the scarab beetle *Cetonia aurata* which was proven to reflect light as a non-diagonal depolarizer.

In this report we present Mueller-matrix images and spectra measured on two selected beetles with cuticles of different complexity. One of the beetles, *Chrysina argenteola*, is a broadband reflector and the other, *Cetonia aurata*, is a narrow-band reflector. First a comparison between images and spectra is performed. We then address the main objective which is to sum decompose Mueller matrices recorded on beetles to identify the character of these biological reflectors. This approach, in which we explore fundamental properties of Mueller matrices from beetles, complements our previous approaches in which we show how Mueller matrices can be used: (I) to derive polarization properties for reflectors of relevance in biology [3] and; (II) to perform electromagnetic modeling to extract structural parameters of relevance for biomimetics [4]. We qualitatively compare decomposition of Mueller-matrix images and spectra from the two near-circularly polarizing beetles studied. We also present quantitative Cloude sum decompositions of Mueller-matrix spectra and images and introduce regression sum decomposition as an alternative.

2. Experimental details

2.1. Instrumentation

Mueller-matrix spectra were recorded with a dual-rotating compensator ellipsometer (RC2, J. A. Woollam Co., Inc.) in the spectral range 245 - 1700 nm and at angles of incidence θ in the range 20 - 75°. Focusing lenses (standard long-focus optics, J. A. Woollam Co., Inc.) were used to reduce spot size to 100 μm or smaller depending on angle of incidence. An xy -translating stage and a camera allowed positioning of the samples with μm resolution in order to find an area on the beetle cuticle free from defects. The focusing lenses introduce a beam spread of around 2° which was found to have negligible influence on the data [4]. Only data in the spectral range 300 - 1000 nm are used in the analysis.

Mueller-matrix images were recorded with an imaging polarimeter described in detail elsewhere [12, 13]. The instrument is equipped with filters and calibrated for wavelengths 532 nm and 633 nm. An objective with 20x magnification and numerical aperture of 0.45 was used in this investigation. With this objective the diameter of the imaged spot was 90 μm and data over the θ -range 0-26° were detected by a 512x512 pixel CCD camera (Hamamatsu). Cloude as well as regression decompositions, both of spectral and image data, were performed with Matlab.

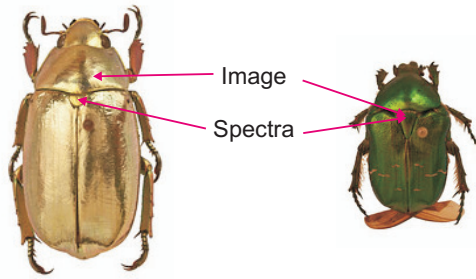


Fig. 1. *C. argenteola* (left) and *C. aurata* (right). The measurement were done on the scutellum (spectra) and in front of the scutellum (images) on *C. argenteola* and on the scutellum on *C. aurata* as marked. The lengths are 29 and 19 mm for *C. argenteola* and *C. aurata*, respectively. (Photos J. Birch)

2.2. The beetle specimens

Figure 1 shows specimens of the two beetles studied. Specimens of *Cetonia aurata* (Linnaeus, 1758) were collected locally whereas the *Chrysina argenteola* (Bates, 1888) specimen was a loan from Museum of Natural History in Stockholm. Mueller-matrix spectra from these beetles have been presented earlier [3, 4]. It should be pointed out that the color of *Cetonia aurata* can vary and beetles with various green, red and even blue color can be found and have been investigated by ellipsometry [14]. All measurements were performed on the scutellum (the small triangular area on the dorsal side of the beetle, see Fig. 1) except the Mueller-matrix images on *C. argenteola*. This beetle was pinned and the pin was a physical hindrance for the objective. To avoid destroying the specimen by removing the pin, measurements were instead performed on the cuticle just behind the head. The beetle cuticle exhibits only minor variations in color and polarizing properties on its dorsal side and the comparison between images and spectra is not affected by measurements at different positions.

3. Theory and modeling

A 4×4 Mueller matrix \mathbf{M} with elements M_{ij} with $i, j = (1, 2, 3, 4)$ provides a description of the linear optical response of a medium and can be defined in reflection, transmission or scattering configurations. The Mueller-matrices presented here are normalized to M_{11} according to $m_{ij} = M_{ij}/M_{11}$ for all elements in \mathbf{M} . A Mueller matrix connects an incident Stokes vector \mathbf{S}_i with an outgoing Stokes vector \mathbf{S}_o according to the relation $\mathbf{S}_o = \mathbf{M}\mathbf{S}_i$ [15].

3.1. Cloude decomposition

The Mueller matrix of a depolarizing optical system can be sum decomposed. As shown by Cloude [6] a depolarizing \mathbf{M} can be represented by a linear combination of up to four non-depolarizing matrices as

$$\mathbf{M} = \lambda_1 \mathbf{M}_1 + \lambda_2 \mathbf{M}_2 + \lambda_3 \mathbf{M}_3 + \lambda_4 \mathbf{M}_4 \quad (1)$$

where the scalars λ_i obey $\lambda_i \geq 0$ and will be defined below. In a Cloude decomposition the objective is to find the λ_i 's and \mathbf{M}_i 's. The procedure is to transform \mathbf{M} to a so called 4×4 covariance matrix \mathbf{C} by the linear operation

$$\mathbf{C} = \sum_{i,j} m_{ij} (\sigma_i \otimes \sigma_j) \quad (2)$$

where the σ_i 's are Pauli spin matrices given by

$$\sigma_1 = \begin{bmatrix} 1 & 0 \\ 0 & 1 \end{bmatrix} \quad \sigma_2 = \begin{bmatrix} 1 & 0 \\ 0 & -1 \end{bmatrix} \quad \sigma_3 = \begin{bmatrix} 0 & 1 \\ 1 & 0 \end{bmatrix} \quad \sigma_4 = \begin{bmatrix} 0 & i \\ -i & 0 \end{bmatrix} \quad (3)$$

If \mathbf{M} is physically realizable, \mathbf{C} is Hermitian positive semi-definite with its four eigenvalues ≥ 0 [6]. Cloude showed that \mathbf{C} can be decomposed as [6]

$$\mathbf{C} = \lambda_1 \mathbf{C}_1 + \lambda_2 \mathbf{C}_2 + \lambda_3 \mathbf{C}_3 + \lambda_4 \mathbf{C}_4 \quad (4)$$

where the λ_i 's are the same as in Eq. (1). The \mathbf{C}_i matrices are found from

$$\mathbf{C}_i = \mathbf{e}_i \mathbf{e}_i^\dagger \quad i = (1, 2, 3, 4) \quad (5)$$

where \mathbf{e}_i are eigenvectors of \mathbf{C} and \dagger indicates the Hermitian conjugate. Once \mathbf{C} in Eq. (4) is found, the inverse operator corresponding to Eq. (2) is applied to \mathbf{C} term by term leading to \mathbf{M} in Eq. (1).

3.2. Regression decomposition

An alternative to a Cloude decomposition is a regression decomposition. Equation (1) is then reformulated as

$$\mathbf{M}^{reg} = \alpha \mathbf{M}_1 + \beta \mathbf{M}_2 + \gamma \mathbf{M}_3 + \delta \mathbf{M}_4 \quad (6)$$

where α, β, γ and δ are fit parameters. The matrices \mathbf{M}_i must in a regression decomposition be known or assumed. If spectral \mathbf{M} are measured, the regression can be performed wavelength-by-wavelength and spectral coefficients $\alpha, \beta, \gamma, \delta$ are obtained. The procedure is to minimize the square root of the sum of squares of all elements in $\mathbf{M} - \mathbf{M}^{reg}(\alpha, \beta, \gamma, \delta)$, i.e. the Frobenius norm

$$F = \|\mathbf{M} - \mathbf{M}^{reg}(\alpha, \beta, \gamma, \delta)\|_F \quad (7)$$

where the fit parameters can be one, two, three or four linear coefficients depending on the complexity of the measured \mathbf{M} and which constraints that are applied to the fit parameters. The quality of the fit depends critically on these constraints and the choice of the \mathbf{M}_i 's. A major difference compared to a Cloude decomposition is that fixed forms of the \mathbf{M}_i 's are imposed over the whole spectrum and do not fluctuate. In a Cloude approach, in which the \mathbf{M}_i 's are based on the eigenvectors of \mathbf{C} on a wavelength-by-wavelength basis, the solutions become less stable. However, a Cloude decomposition provides important input to a regression decomposition in terms of the number of non-zero eigenvalues and, in this special case, also the forms of the elementary polarizing components, i.e. the \mathbf{M}_i 's. In the example on decomposition of data from *C. aurata* presented in the result section, a Cloude decomposition results in two non-zero λ_i 's and a fit can be performed with the two fit parameters α and β assuming $\gamma = \delta = 0$. Furthermore an eigenvector analysis, as well as images of *C. aurata* [11], suggests the use of an ideal mirror and a left-handed circular polarizer as the corresponding \mathbf{M}_i 's. If the sum constraint $\alpha + \beta + \gamma + \delta = 1$ also is used only α will be a fit parameter in the regression as β follows from $\beta = 1 - \alpha$ in this case.

4. Results and discussion

4.1. Primary data - examples

Several specimens of the beetles were studied at various setting of the instruments. Here a selection of primary data are shown to demonstrate data qualities and general optical features of the cuticles of beetles.

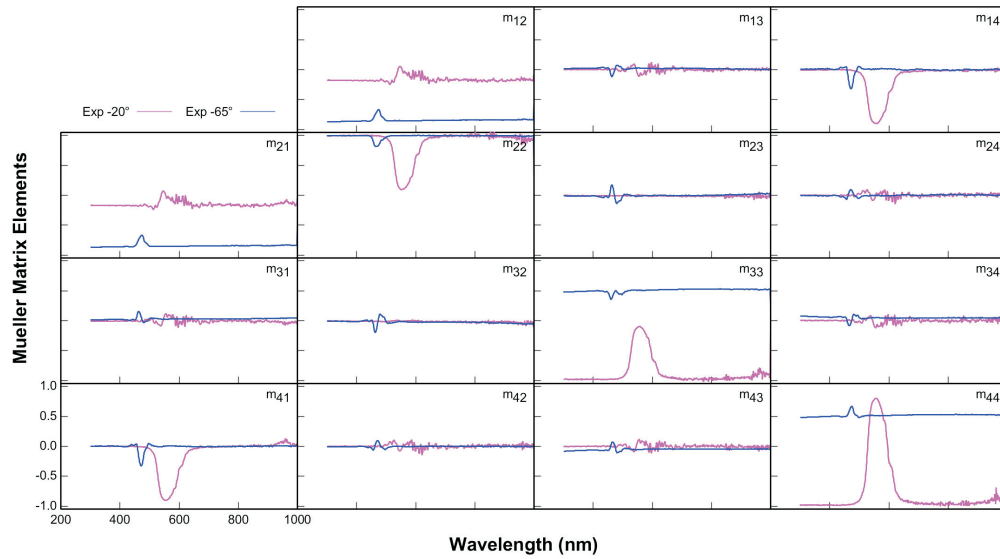


Fig. 2. Normalized Mueller-matrix spectra measured at $\theta = 20^\circ$ and 65° on a *C. aurata* beetle. The scale for all elements is the same as shown for m_{41} .

C. aurata is a narrow-band reflector as seen in the spectral Mueller matrices shown in Fig. 2 for $\theta = 20^\circ$ and 65° . We observe that the spectral features at an angle of incidence of 20° are largest around 550 nm, e.g. in element m_{41} , and that they shift to shorter wavelengths and become much smaller at $\theta = 65^\circ$ which is further discussed and modeled elsewhere [3, 4]. These major features seen in m_{41} , m_{14} and in the diagonal elements are near-symmetric with a width at half maximum of around 55 nm (at $\theta = 20^\circ$) and with some weak oscillations on the long-wavelength side. The features are identified as Bragg resonances and correspond to that the beetle when illuminated with unpolarized light reflects green light with near-circular left-handed polarized light at small θ . For other wavelengths the beetle appears like a dielectric mirror [3].

C. argenteola is a broad-band reflector and also exhibits left-handed polarization features at $\theta = 20^\circ$ as seen in Fig. 3. The sign and magnitude of m_{41} show that the reflected light is left-handed and near-circularly polarized when the beetle is illuminated with unpolarized light. However, the cuticle also shows right-handed polarization features depending on wavelength and angle of incidence. For large θ , m_{41} becomes positive and the reflected light is right-handed polarized for wavelengths larger than 500 nm at $\theta = 65^\circ$. The Mueller-matrix spectra in Fig. 3 are therefore more complex than those for *C. aurata* and have spectral features in the whole visible range explaining the gold-like color of *C. argenteola* compared to the green color of *C. aurata*. In addition to the major features discussed above, we also observe oscillations in the *C. argenteola* spectra which are more pronounced than in spectra from *C. aurata*. These oscillations are due to interference between the front side and the back side of the cuticle.

Figure 4 shows Mueller-matrix images of *C. aurata* measured at wavelengths 532 nm and 633 nm. In both cases an irregular patterning can be seen in the images. At 532 nm the off-diagonal elements are close to zero, except m_{41} and m_{14} which have small negative values, and the diagonal elements resemble those of a mirror in reflection mode. Recall that a Mueller matrix of an ideal mirror has diagonal elements [1,1,-1,-1] and the remaining elements zero [15]. Notice the minus signs in the last two diagonal elements which are due to that the Verdet convention is used for the interface reflection coefficients [16]. At 633 nm, the diagonal elements

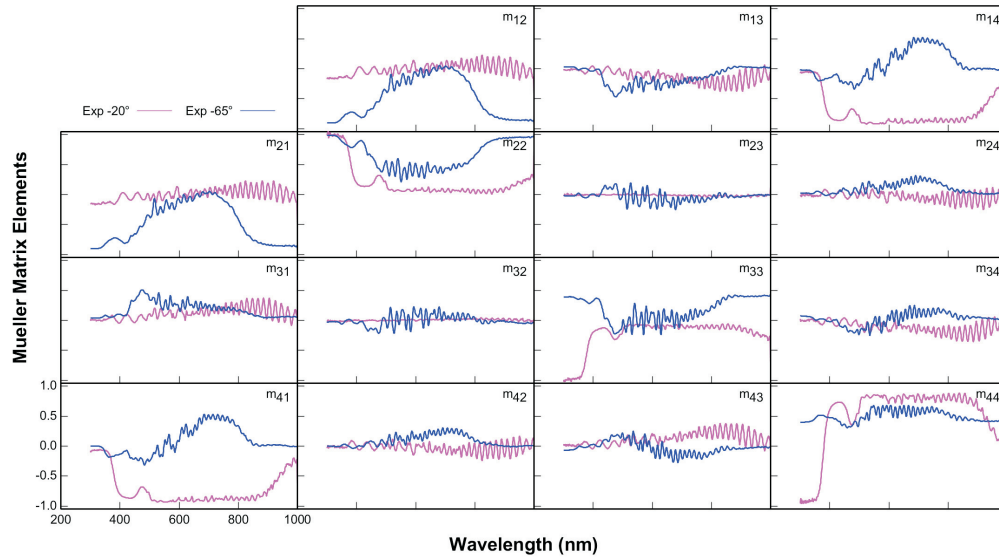


Fig. 3. Normalized Mueller-matrix spectra measured at $\theta = 20^\circ$ and 65° on a *C. argenteola* beetle. The scale for all elements is the same as shown for m_{41} .

are different. The elements m_{22} and m_{33} have decreased in magnitude but with signs preserved. Element m_{44} has decreased and has become slightly positive in some small areas. Other changes are that m_{41} and m_{14} are more negative indicating larger left-handed polarizing effects. In fact when changing from 532 nm to 633 nm, the Mueller matrix changes from a matrix resembling a mirror to a matrix closer to that of a circular polarizer. The latter ideally has $m_{11} = m_{44} = 1$ and $m_{14} = m_{41} = -1$ if left-handed and remaining elements zero. When comparing the images in Fig. 4 with the spectra in Fig. 2, it should be considered that the images are averaged over the field of view (angle of incidence) which corresponds to an angle range of $0-26^\circ$ with the objective used. Furthermore the spectral data in Fig. 2 are recorded at $\theta = 20^\circ$. By considering a shift of features towards longer wavelengths for smaller θ as in the images, we find an excellent qualitative agreement between the spectral and image Mueller-matrix data. It should be pointed out that optimal wavelengths for the image recording were not available and 532 nm and 633 nm is on the short and long wavelengths side of the Bragg resonance, respectively. Ideally it would have been better to measure at the resonance as well as far away from it, whereby a more distinct difference between the two characteristics of the cuticle would have been observed.

Figure 5 shows Mueller-matrix images of *C. argenteola* measured at wavelengths 532 nm and 633 nm. At both wavelengths, large negative values on m_{41} and m_{14} elements are observed. The remaining off-diagonal elements are small as well as elements m_{22} and m_{33} whereas m_{44} is large and positive. The Mueller matrices thus exhibit properties of a circular polarizer. The qualitative agreement with the spectra in Fig. 3 is excellent. However, a closer inspection of some of the off-diagonal elements, e.g. m_{43} , reveals a pattern which is very regular and of size of the order of 5-6 μm . Such patterns have been observed in other chrysina beetles and have been assigned to cusp-like structures in the cuticle surface [17, 18].

4.2. Cloude decomposition of measured Mueller-matrix spectra

A Cloude decomposition applied to the spectral Mueller matrix for *C. aurata* at $\theta = 20^\circ$ in Fig. 2 results in the four eigenvalues shown in Fig. 6(a). Two eigenvalues are very close to zero

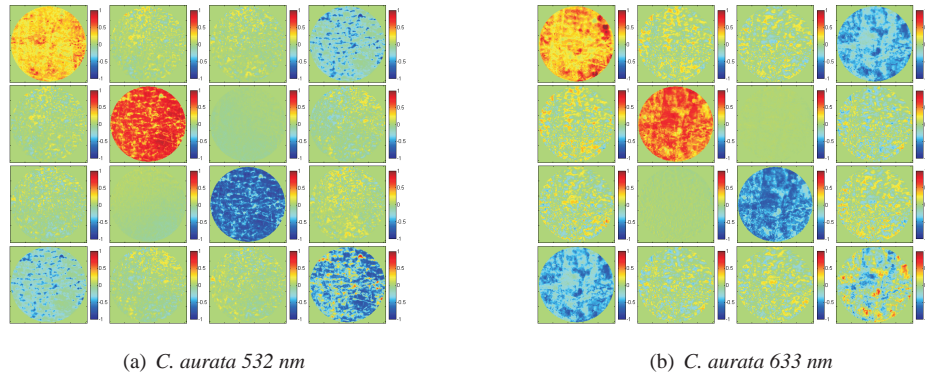


Fig. 4. Normalized Mueller-matrix images of *C. aurata* at wavelengths 532 nm and 633 nm.

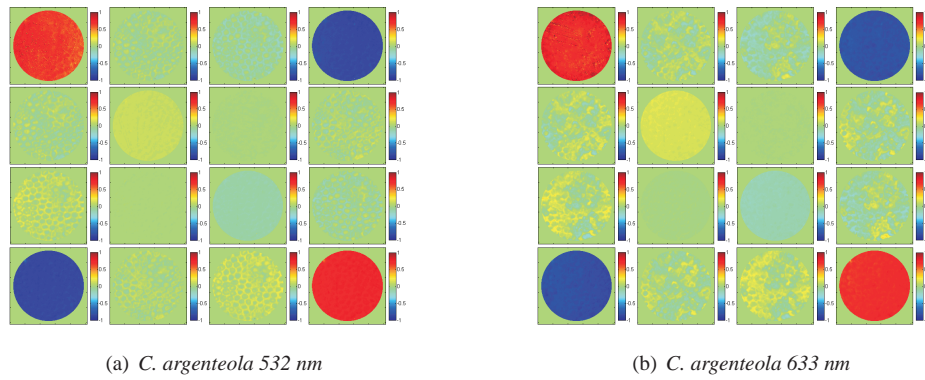


Fig. 5. Normalized Mueller-matrix images of *C. argenteola* at wavelengths 532 nm and 633 nm.

(<0.01 in most of the spectral region) and this matrix can thus be approximately decomposed as

$$\mathbf{M} \approx \lambda_1 \mathbf{M}_1 + \lambda_2 \mathbf{M}_2 + 0 \cdot \mathbf{M}_3 + 0 \cdot \mathbf{M}_4 \quad (8)$$

where λ_1 and λ_2 depend on the wavelength as in Fig. 6(a) whereas λ_3 and λ_4 are set to zero. A technical detail to mention is that an eigenvalue determination provides values on eigenvalues independent of the type of its corresponding eigenvector and will be sorted with λ_1 , λ_2 , λ_3 and λ_4 having descending values. λ_1 will therefore always be largest. However, when solving for eigenvalues, starting at one end of a spectrum, an eigenvalue associated with a specific eigenvector may decrease and may at some wavelength become smaller than another eigenvalue. This is the case for the results presented in Fig. 6(a) and occurs at the two wavelengths where the eigenvalues cross (529 and 593 nm). For wavelengths shorter than 529 nm and longer than 593 nm, λ_1 which in these ranges is associated with \mathbf{M}_1 is larger than λ_2 (associated with \mathbf{M}_2), whereas in the range 529-593 nm, the eigenvalues λ_1 and λ_2 change roles and λ_2 instead of λ_1 is associated with \mathbf{M}_1 . We have interchanged the data for λ_1 and λ_2 in this spectral range to facilitate comparison with fit parameters in the regression decomposition in the next section.

From an eigenvector analysis of the covariance matrix of \mathbf{M} using Eq. (5) and the inverse of Eq. (2), the matrices \mathbf{M}_i in Eq. (8) are found to be close to an ideal dielectric mirror

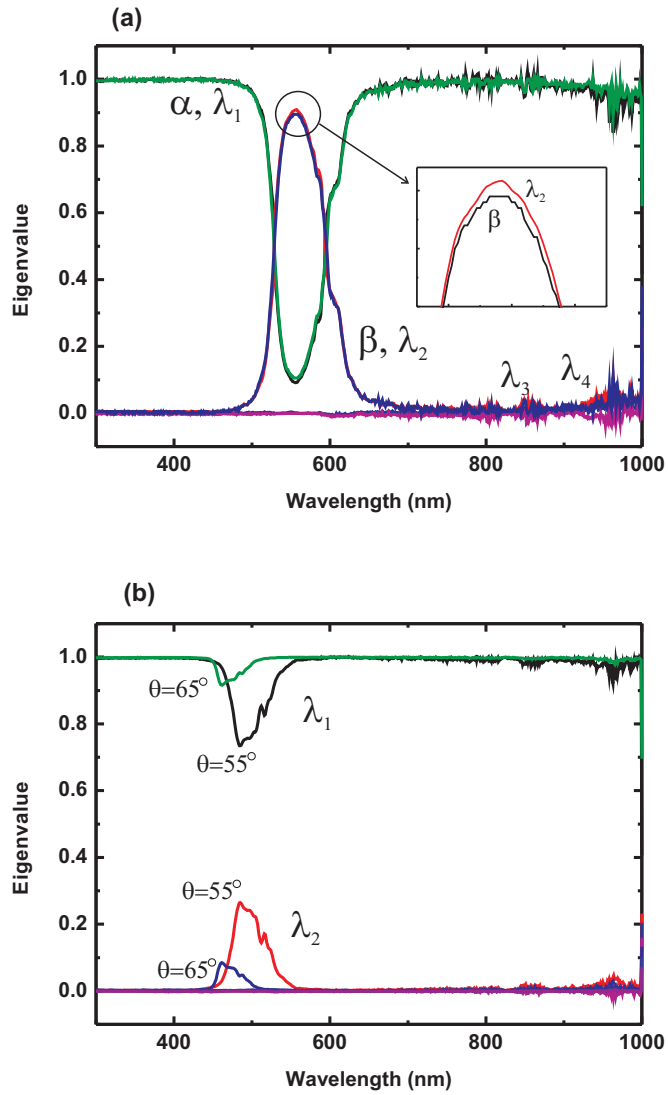


Fig. 6. (a) The four eigenvalues obtained by a Cloude decomposition of Mueller matrices measured on *C. aurata* at $\theta = 20^\circ$. The decomposition fit parameters α and β from Eq. (7) are also shown. (b) The four eigenvalues obtained by a Cloude decomposition of Mueller matrices measured on *C. aurata* at $\theta = 55^\circ$ and $\theta = 65^\circ$.

(\mathbf{M}_1), a left-handed circular polarizer (\mathbf{M}_2), a half-wave plate oriented with azimuth 45° (\mathbf{M}_3) and a right-handed circular polarizer (\mathbf{M}_4). However, as only the first two eigenvalues are significantly different from zero, in the first approximation, only \mathbf{M}_1 and \mathbf{M}_2 contribute and Eq. (8) can be written out as

$$\mathbf{M} \approx \lambda_1 \begin{bmatrix} 1 & 0 & 0 & 0 \\ 0 & 1 & 0 & 0 \\ 0 & 0 & -1 & 0 \\ 0 & 0 & 0 & -1 \end{bmatrix} + \lambda_2 \begin{bmatrix} 1 & 0 & 0 & -1 \\ 0 & 0 & 0 & 0 \\ 0 & 0 & 0 & 0 \\ -1 & 0 & 0 & 1 \end{bmatrix} \quad (9)$$

where matrices for an ideal mirror and an ideal left-handed circular polarizer are replacing \mathbf{M}_1 and \mathbf{M}_2 , respectively, and λ_1 and λ_2 are the eigenvalue spectra in Fig. 6(a). By observing the eigenvalues in Fig. 6(a), we find that \mathbf{M}_1 is dominating except in a spectral band around 550 nm where \mathbf{M}_2 is large. We refer to this band as the Bragg regime. We conclude that a green specimen of *C. aurata* at near-normal incidence reflects like an ordinary dielectric mirror for blue (<500 nm) and red (>600 nm) light, whereas for green light it appears as a left-handed circular polarizer.

An interesting observation is that \mathbf{M} in Eq. (9) represents a non-diagonal depolarizer [11, 19] and is also referred to as a Stokes non-diagonalizable Mueller matrix. Such depolarizers will depolarize all incident states except one. For *C. aurata* this special incident state is left-handed circularly polarized light. All other states will be depolarized. Samples with such Mueller matrices are rare as pointed out by Ossikovski et al. [11].

In Fig. 6(b), the eigenvalues for \mathbf{M} measured at $\theta = 55^\circ$ and $\theta = 65^\circ$ show that at larger angles of incidence, λ_2 is smaller in the Bragg regime compared to at near-normal incidence. The conclusion is that \mathbf{M} of *C. aurata* at larger angles of incidence is dominated by \mathbf{M}_1 and thus appears mainly as a mirror with a weak contribution from a circular polarizer in a narrow spectral range. If the data are extrapolated to grazing incidence, λ_1 approaches unity and \mathbf{M} corresponds to a non-depolarizing reflector, in this case a dielectric mirror.

Cloude decompositions of the Mueller-matrix data measured at $\theta = 20^\circ$ and $\theta = 65^\circ$ on *C. argenteola* in Fig. 3, results in eigenvalues as shown in Fig. 7 where an eigenvalue order correction has been done at 380 nm for the $\theta = 20^\circ$ results. At near-normal incidence ($\theta = 20^\circ$), the eigenvalues λ_1 and λ_2 are dominating but λ_3 and λ_4 both exhibit a slow increase with wavelength in the visible spectral range and for wavelengths larger than 900 nm they increase further. Therefore, if we assume $\lambda_3 = \lambda_4 = 0$, the data in Fig. 3 recorded at $\theta = 20^\circ$ can be decomposed, at least in the visible range, as in Eq. (9) by using eigenvalues λ_1 and λ_2 from Fig. 7(a). Below 300 nm as well as above 1000 nm, λ_1 is close to unity and the other eigenvalues are small and are not shown here. Result for *C. argenteola* and *C. aurata* are therefore in principle very similar at this angle of incidence. Notice, however, that λ_2 is non-zero over most of the visible spectral range for *C. argenteola* compared to *C. aurata* for which λ_2 is non-zero only in a narrow spectral range around 550 nm.

At $\theta = 65^\circ$, λ_1 and λ_2 are dominating for *C. argenteola* but λ_3 is non-zero for wavelengths in the 500-700 nm range whereas $\lambda_4 = 0$ over the spectral range used in this study. A third, so far unidentified, matrix \mathbf{M}_3 should be used in Eq. (8). A more detailed study of the decomposition of spectral data from *C. argenteola* will be presented elsewhere.

4.3. Regression sum decomposition of spectra

Here we demonstrate regression decomposition of spectral \mathbf{M} measured on *C. aurata*. A single-parameter approach is used with α as fit parameter in Eq. (7). $\gamma = \delta = 0$ is assumed and with the constraint $\sum \lambda_i = 1$ we have $\beta = 1 - \alpha$. An ideal mirror and a left-handed circular polarizer as used in Eq. (9) are assumed for \mathbf{M}_1 and \mathbf{M}_2 , respectively. The regression analysis is performed

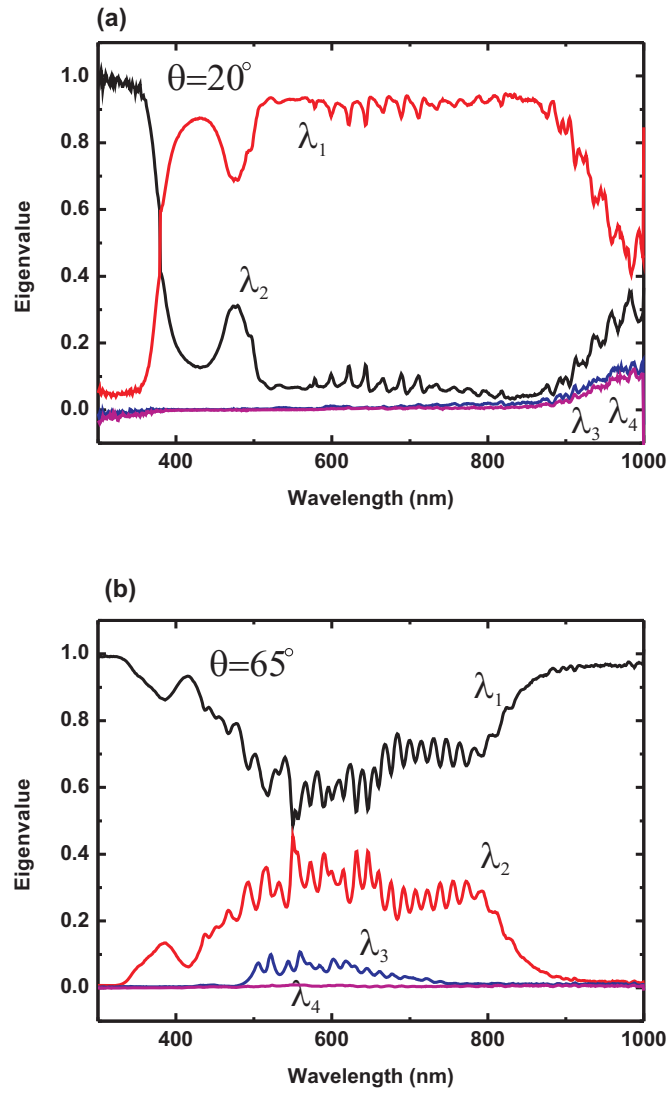


Fig. 7. The four eigenvalues obtained by a Cloude decomposition of Mueller matrices measured on *C. argenteola* at (a) $\theta = 20^\circ$ and (b) $\theta = 65^\circ$.

in Matlab using the least-square regression algorithm.

Figure 6(a) shows α and $\beta = 1 - \alpha$ obtained in the regression analysis of \mathbf{M} recorded on *C. aurata* at $\theta = 20^\circ$ under conditions described above. These results are very close to those from the Cloude decomposition. Notice that the difference in the two approaches are that in a regression decomposition, the fitted linear coefficients α and β are determined under an assumption of specific forms of the matrices \mathbf{M}_1 and \mathbf{M}_2 , whereas in a Cloude decomposition the true eigenvalues are determined independently of \mathbf{M}_1 and \mathbf{M}_2 . Furthermore there are no problems with magnitude sorting of eigenvalues in a regression decomposition as it is in a Cloude decomposition.

For larger angles of incidence, the regression decomposition becomes more complex and circular polarizer matrices \mathbf{M}_i may have to be replaced by matrices corresponding to elliptical polarizers. Furthermore, for *C. argenteola* we find three non-zero eigenvalues and the regression decomposition becomes more complex. An extended regression sum decomposition of Mueller-matrix data of beetle cuticles will be presented elsewhere.

4.4. Cloude and regression sum decomposition of images

In Fig. 8, images for the spatial distributions of the four eigenvalues from a Cloude decomposition of the Mueller-matrix images at 532 nm for *C. aurata* are shown. λ_1 and λ_2 exhibit patterning telling us that the surface is spatially inhomogeneous. The patterning can also be seen in the smaller eigenvalues λ_3 and λ_4 . λ_4 is very small and set to zero in the regression. λ_1 and λ_2 varies between 0.5 and 1 and between 0 and 0.5, respectively, and should together with the small value of λ_3 add up to 1 in each point if $\lambda_4 = 0$ is assumed. It should be emphasized here that eigenvalue sorting by the magnitude occurs in the Cloude decomposition as was already discussed in section 4.2. In each pixel $\lambda_1 > \lambda_2$ and consequently λ_1 and λ_2 do not show the fraction of contributions from their corresponding eigenvectors. This property of the Cloude decomposition procedure is a hindrance for an easy interpretation of eigenvalue images. It would be very elaborate to manually do an eigenvalue correction as was done for the spectral data.

The result of a regression decomposition at 532 nm assuming three basic components, an ideal mirror, a circular polarizer and a half-wave plate with coefficients α , β and γ , respectively, in Eq. (6) is also shown in Fig. 8. The fact that a specific Mueller matrix is assigned to each eigenvalue guarantees that the eigenvalues represent the weights of the basic optical component corresponding to the Mueller matrices used. We notice that the mirror dominates with values of $\alpha = 0.5$ or larger in most pixels, whereas β mostly has values < 0.3 except in some areas where values up to 0.8 are found. The contribution from a quarter-wave plate corresponding to γ is very small in accordance with the results from the Cloude decomposition. The discrepancies between a Cloude and a regression decomposition is clearly seen if λ_1 and λ_2 images are compared with α and β images.

Cloude and regression decompositions at 633 nm for *C. aurata* are shown in Fig. 9. Also here λ_3 and λ_4 are close to zero and a weak patterning can be seen. λ_1 and λ_2 exhibit pronounced patterning. In the same way as for the images at 532 nm, the eigenvalue sorting issue complicates the interpretation of the eigenvalues. However, on average λ_1 is smaller and λ_2 is larger compared to the corresponding λ_1 and λ_2 at 532 nm. The regression analysis shows that a mirror dominates but to a smaller extent as α is smaller on average and β larger compared to values at 532 nm. This is due to the wavelength of 633 nm being closer to the Bragg resonance wavelength than the wavelength of 532 nm is. Also here γ is very small. Ideally it would have been best to record images at the resonance wavelength where the circular polarizer should dominate.

Cloude and regression decompositions at 532 nm for *C. argenteola* are shown in Fig. 10,

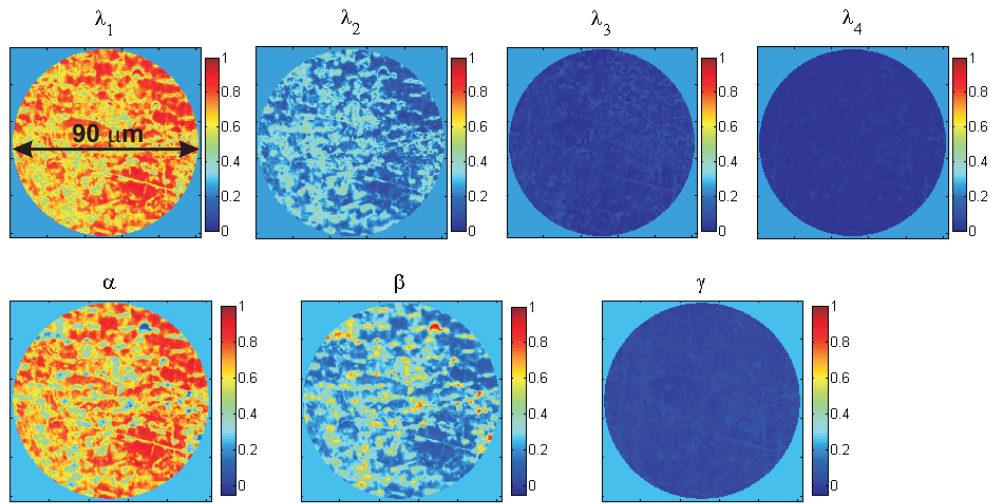


Fig. 8. The top row shows the spatial variation of the four eigenvalues obtained by a Cloude decomposition of the Mueller-matrix image at 532 nm on *C. aurata* in Fig. 4(a). The bottom row shows the spatial variation of a mirror, a circular polarizer and a half-wave plate corresponding to α , β and γ in Eq. (6).

where we observe one dominating eigenvalue, a second smaller eigenvalue and two eigenvalues close to zero. α and β from a regression sum decomposition in a circular polarizer and an ideal mirror are also shown. The fit parameter γ corresponding to a quarter-wave plate is very small. The fit parameter β dominates and we conclude, from the decomposition of Mueller-matrix image data taken at the wavelength of 532 nm, that reflection at near-normal incidence for *C. argenteola* can be represented by a circular polarizer with a minor contribution from a plane mirror. Notice that the eigenvalue sorting problem does not affect the comparison between Cloude and regression results in this case as λ_1 (and β) are 0.8 or larger over the whole measurement spot. The weak pattern observed in \mathbf{M} in Fig. 5 for *C. argenteola* is also visible in the λ_1 , λ_2 , λ_3 , α and β images in Fig. 10. Similar patterns have been observed in several beetles including *Chrysina gloriosa*, *Pseudochalcothea auripes* and *Protaetia (Potosia) cuprea* [13, 18]. The results for *C. argenteola* at 633 nm are almost identical to those at 532 nm and are therefore not shown.

We can conclude that the regression decomposition of Mueller-matrix image data shows an excellent agreement with the regression decomposition of spectral data for *C. argenteola*. However, when using a Cloude decomposition, interpretations may be complicated by the size ordering of eigenvalues in spectra and images.

4.5. General discussion

In this report both spectral and image Mueller matrices measured with comparable spot sizes are presented and compared. Recall that images are averages over incident angles but with spatial resolution, whereas spectra are spatial averages but with angle resolution. In spite of this the qualitative agreements are very good. This is particularly the case for *C. argenteola* which is due to the fact that the cuticle spatially appears to be very homogeneous with only a weak pattern observed. The point-to-point variation is therefore small and the spectra are not affected by lateral variations on the cuticle to any larger extent. The averaging over angles in the images

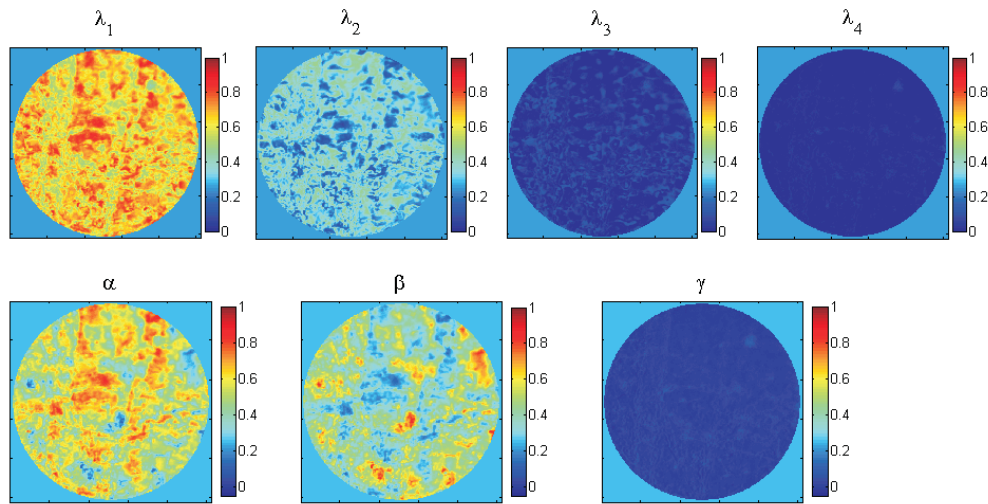


Fig. 9. The top row shows the spatial variation of the four eigenvalues obtained by a Cloude decomposition of the Mueller-matrix image at 633 nm on *C. aurata* in Fig. 4(b). The bottom row shows the spatial variation of a mirror, a circular polarizer and a half-wave plate corresponding to α , β and γ .

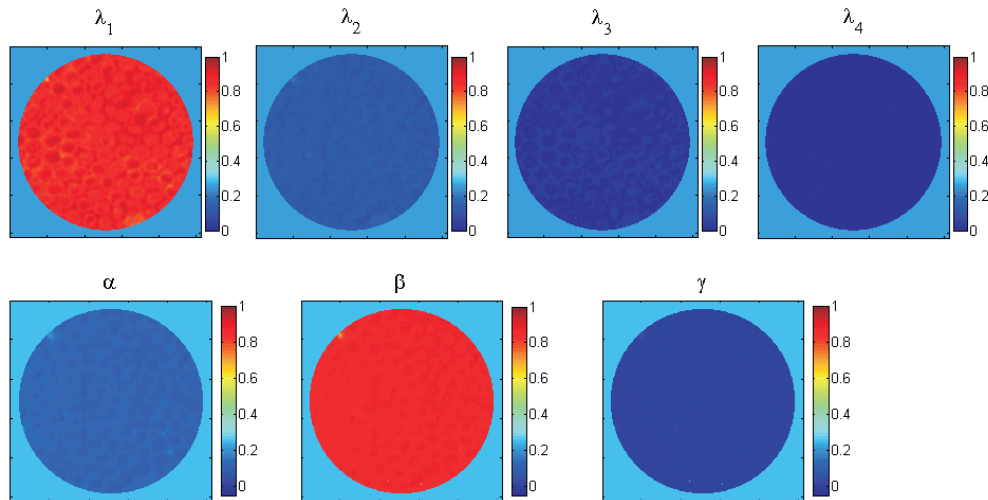


Fig. 10. The top row shows the spatial variation of the four eigenvalues obtained by a Cloude decomposition of the Mueller-matrix image at 532 nm on *C. argenteola* in Fig. 5(a). The bottom row shows the spatial variation of a mirror, a circular polarizer and a half-wave plate corresponding to α , β and γ . Notice that the sorting of eigenvalues after magnitude results in that λ_1 is largest, whereas for the regression β as defined in Eq. (6) is largest.

also has small influence as for near-normal incidence, the reflection coefficients and thereby the Mueller-matrix elements, depend only weakly on incident angle as verified by simulations (not shown here). For *C. aurata* the agreement between the image and spectral data is also surprisingly good in spite of the patterning observed in the images.

The fact that patterning is observed in the images raises the question whether the depolarization properties of the measured Mueller matrices is due to lateral inhomogeneities implying that several types of Mueller matrices within the beam spot contribute or whether the depolarization is an intrinsic property of the cuticle structure. In a patterned-based model the cuticle would then have at least two types of domains: mirror domains and circular polarizer domains. At the Bragg resonance wavelength the contributions from circular polarizer domains are largest and far away from the resonance, mirror domains dominate. At the resonance, λ_2 is 0.9 or larger which implies that more than 90% of the contributions are from circular polarizer domains. However, it should be considered that at small angles the reflectance from a dielectric mirror is much smaller than that from a Bragg reflector at resonance. If we use an average refractive index of 1.51 and a in-plane birefringence of 0.07 for a chiral stack [4], we find at $\theta = 0^\circ$, a Bragg reflectance of 0.46 for left-handed polarized light using simple expressions for Bragg reflection [20] and a mirror reflectance of 0.04 using Fresnel's reflection laws. Simulations show that these values will be reduced a few percent if θ is increased to 20° . If we assume that the epicuticle also affects the two types of domains in similar ways, we can estimate that the circular polarizer domains have more than 10 times larger reflectance than the mirror domains. If we now in a numerical example assume that 50% of the surface has circular polarizer domains we can add the two matrices in Eq. (9) with equal weights and unnormalized, i.e. with all elements multiplied with $m_{11} = 0.04$ and $m_{11} = 0.46$ for the mirror and circular polarizer, respectively, and then normalize the resulting \mathbf{M} . A value of $m_{41} = 0.92$ is then found which should be compared to $m_{11} \approx 0.9$ observed experimentally for *C. aurata* at resonance. Thus we can not conclude that a major fraction of the cuticle is circularly polarizing as Mueller-matrix normalization strongly emphasizes the circularly polarizing domains due to their larger reflectance. In other words, a cuticle which geometrically is dominated by domains reflecting as mirrors may visually appear as a circular polarizer in the Bragg regime.

The depolarization may also be due to an intrinsic effect. The cuticle surface would then be spatially homogeneous with only one type of basic structure which, depending on wavelength, acts either as a mirror, as a circular polarizer or as a hybrid resembling properties of an elliptic polarizer. Different interference mechanisms in the Bragg structure will dominate at different wavelengths and not different spatial domains as in the pattern-based model. A possibility would be to model the spectral Mueller matrices as elliptic polarizers with a wavelength-dependent ellipticity and azimuth.

Interestingly, the images on *C. argenteola* in Fig. 10 show very weak patterning which may support the intrinsic-based model or at least that the cuticle to a very large extent is homogeneous. The patterned-based model is supported by Mueller-matrix images measured close to the resonance wavelength [11] which exhibits patterning with two areas with approximately the same coverage. Clearly the data presented in our work are not conclusive and further investigations are needed to fully determine the character of the cuticles studied.

From a methodological point of view it would be favorable to be able to determine spectral data at normal-incidence for increased accuracy in the decomposition. Another valuable improvement would be to record images at additional wavelengths to get a more complete picture of the cuticle reflection. Further possibilities are to reduce θ averaging in the images by using spatial filters in the beam so that one θ at the time is probed.

In Figs. 6 and 7 noise can be observed in the eigenvalues for long and short wavelengths, respectively. Furthermore, λ_4 exhibit negative values, albeit noisy, in some spectral regions in

spite of that the covariance matrix \mathbf{C} should be positive semi-definite. The noise can be traced back to the primary data and can be seen in Figs. 2 and 3. The data become noisy because the Mueller-matrix elements are normalized to the overall reflectance which is very low at these wavelengths. The negative value of λ_4 is due to the fact that the eigenvalue algorithm uses the $\Sigma\lambda_i = 1$ and $\lambda_4 = 1 - \lambda_1 - \lambda_2 - \lambda_3$, i.e. a residue. Noise in the data and possibly small systematic errors can then lead to negative values of λ_4 .

In some Mueller-matrix elements oscillations are clearly visible, especially for *C. argenteola* at $\theta = 65^\circ$. The origin of these oscillations are not addressed here, but they are due to Fabry-Perot resonances between parallel interfaces, which depend on the cuticle thickness and structure. For opaque cuticles like in *C. aurata* the oscillations become very weak or vanish completely. However, if sufficiently large they can be used to determine cuticle thickness and also to explore cuticle structure [21, 22].

5. Concluding remarks

Mueller-matrix spectra as well as Mueller-matrix images from cuticles of the beetles studied can be Cloude decomposed and their corresponding covariance matrices are found to exhibit two non-zero dominating eigenvalues. For more complex beetle cuticles additional eigenvalues are found to be non-zero.

An eigenvector analysis of spectral data suggests that a mirror and a circular polarizer are basic optical components of the measured Mueller matrices and a sum decomposition reveals that in simple cases these two components in a first approximation sufficiently can describe the biological reflectors studied.

It is also possible to do a regression-based decomposition assuming a set of basic optical components with a fit with no constraints on the fit parameters α , β , γ and δ . Alternatively it is possible to employ various constraints like $\alpha + \beta + \gamma + \delta = 1$, $\alpha = 1 - \beta$, $\gamma = \delta = 0$, $0 \leq \alpha, \beta, \gamma, \delta \leq 1$ or combinations of these constraints.

A comparison between a Cloude and a regression decomposition shows that a regression analysis is more stable and fit parameters have fixed associations to eigenvectors of the covariance matrix of the studied Mueller matrix, whereas in a Cloude analysis, the associations among eigenvectors and eigenvalues may vary over a spectrum or an image. The disadvantage with a regression decomposition is that the basic optical components corresponding to eigenvectors must be determined a priori.

Acknowledgments

This work is dedicated to the memory of our colleague Antonello De Martino who suddenly passed away during the preparation of the manuscript. Specimens of *C. aurata* were kindly provided by Jan Landin and specimens of *C. argenteola* were on loan from Museum of Natural History in Stockholm. Sandeep Singh is acknowledged for help with some of the image measurements and Jens Birch for providing photos of the beetles. This work is supported by grants from the Swedish Research Council and from Carl Tryggers foundation. Knut and Alice Wallenberg foundation is acknowledged for support of instrumentation.